Research paper

Revisiting excitation force estimation in WECs: On the (mis)use of structure-based estimation approaches

Demián García-Violini [a,b,c,*], Nicolás Faedo [d], Yerai Peña-Sanchez [e], Vincenzo Nava [f], John V. Ringwood [c]

[a] CONICET, Avda. Rivadavia 1917, Ciudad Autónoma de Buenos Aires, C1033AAJ, Argentina
[b] Departamento de Ciencia y Tecnología, Universidad Nacional de Quilmes, Roque Sáenz Peña 352, Bernal, B1876, Buenos Aires, Argentina
[c] Centre for Ocean Energy Research (COER), Dept. of Electronic Engineering, Maynooth University, Co. Kildare, K71 2AA, Ireland
[d] Marine Offshore Renewable Energy Lab., Department of Mechanical and Aerospace Engineering, Politecnico di Torino, Corso Duca degli Abruzzi, 24, Torino, 10129, Italy
[e] Mondragon University, Loramendi Kalea, 4, Arrasate, 20500, Guipuzkoa, Spain
[f] Basque Center for Applied Mathematics (BCAM), Mazarredo Zumarkalea, 14, Bilbao, 48009, Bizkaia, Spain

ARTICLE INFO

ABSTRACT

Wave excitation force (torque) estimators, vital in wave energy systems, generally combine the nominal representation of a wave energy converter (WEC) with an excitation force (perturbation) model. Thus, this model-based estimation approach, grounded in the internal model principle, often employs two perturbation models: (i) the harmonic oscillator structure, prevalent in literature, assuming sinusoidal signals; and (ii) the integrator (random walk) scheme, assuming unit step-like signals. These models comprehensively represent a specific family of estimators, as discussed in this study. However, both models may struggle to capture the irregular (stochastic) nature of ocean waves. This study challenges the prevailing assumption that the harmonic oscillator structure, selected for its resemblance to ocean wave oscillations, is inherently the optimal choice. This study provides a rigorous discussion on convergence conditions. Thus, is shown that, while the harmonic oscillator can be highly effective under specific conditions, the random walk structure, despite its simplicity, can surpass the performance of the harmonic oscillator scheme. Formal proofs support this argument, emphasising the effectiveness of the harmonic oscillator can be guaranteed with periodic signals.

1. Introduction

The urgent need for a global energy transition has become a paramount concern, driven by the detrimental impact of fossil fuels on the environment (Guo and Ringwood, 2021). Recognising the imperative to shift the current energy source mix, several countries and organisations worldwide have identified this as a critical milestone for a sustainable future (International Energy Agency, 2019).

While R&D efforts have predominantly focused on established renewable energy technologies, like wind and solar power, the untapped potential of ocean wave energy remains a promising and relatively unexplored frontier. With an estimated resource capacity of around 1.8 $\cdot 10^4$ TWh (Guo and Ringwood, 2021), ocean waves have the capacity to supply over 12% of the current global energy consumption, offering a substantial contribution to a clean energy transition.

Optimising the performance of wave energy converters (WECs) is pivotal in harnessing the energy potential of ocean waves (Ringwood et al., 2014). These devices are designed to extract energy from waves, making optimal control strategies for WECs essential (Ringwood et al., 2014). However, many advanced control strategies rely on precise knowledge of the force that waves exert on the WEC, commonly referred to as the wave excitation force[1] (García-Violini et al., 2020; Li and Patton, 2023). Hence, given the intrinsic unmeasurability of the excitation force, an alternative approach is employed: estimation of excitation force using observable parameters, such as WEC motion (position, velocity, etc.) (Peña-Sanchez et al., 2019b). This process typically involves an unknown input observer strategy to derive accurate estimates (Nguyen and Tona, 2018).

Several techniques have been proposed in the literature for estimating wave excitation force in WEC systems (Peña-Sanchez et al.,

---

2019b; Abdelrahman and Patton, 2020), with many of them based on Luenberger structures (Luenberger, 1971). In particular, it is worth noting that the study in Abdelrahman and Patton (2020) can be complemented by the insights provided in this study, as discussed in the following paragraphs, but especially in Section 4. These estimators are designed using an extended system, which, based on the internal model principle (IMP) theory (Francis and Wonham, 1976), incorporates a nominal representation of the WEC system, alongside an implicit form deterministic model characterising the excitation force structure. Two particular perturbation models have been prevalent in the literature for designing these observers. The first, known as the harmonic oscillator structure, is inspired by the inherent oscillatory nature of ocean waves. This model, widely adopted and extensively explored in the wave energy field (Ling and Batten, 2015; Kracht et al., 2015; Garcia-Abril et al., 2017; Hillis et al., 2020; García-Violini et al., 2021; Zhang et al., 2023), is, to the best of the authors' knowledge, the most widespread and widely used representation for wave excitation estimation in WEC systems. However, these references lack comprehensive analytical proof. The second predominant model is based on the random walk scheme (Nguyen and Tona, 2018; Davis and Fabien, 2020), which is essentially an integration-based estimation scheme, with the assumption that the process to be estimated evolves slowly, allowing it to be approximated as a combination of sequential step signals. Among these two deterministic models, the integration-based scheme can be indicated as the simplest estimation structure, as further discussed in Section 3.1. It must be noted that, as subsequently discussed in this study, both the harmonic oscillator and the random walk structures are effective and general descriptors of the model family defined by the IMP for unknown input estimators. Consequently, these structures serve as suitable candidates for the family of IMP-based estimators, making them well-suited for performance assessment.

The IMP posits that the signal under consideration, whether for tracking, rejection, or estimation purposes within a given application framework, inherently possesses an internal model (generating polynomial) (Goodwin et al., 2001) that aligns with specific assumptions concerning the unknown input. For example, in the context of the harmonic oscillator model, the assumption is that the excitation force of the wave constitutes a periodic sinusoidal-based signal. Conversely, in the random walk scheme, the assumption is that the process to be estimated undergoes gradual changes, allowing it to be modelled as a sequential combination of step signals. It is essential to note that the efficacy of the IMP theory hinges on the fulfilment of these underlying assumptions. When these assumptions are perfectly met, the IMP asymptotically ensures convergence with null error (in steady-state). Nevertheless, it is crucial to acknowledge a significant challenge stemming from the irregular stochastic nature of ocean waves (Falnes, 2002). The wave excitation force, driven by complex and dynamic wave patterns, often deviates from the strict periodicity or step-like behaviour assumed by these models. While these models can provide useful approximations at times, they may not fully capture the nuanced and intricate nature of the excitation force, which is inherently influenced by the unpredictable and variable conditions of the ocean environment.

The primary contribution of this paper is a critical exploration and substantiation of the estimation schemes employed in WEC systems. Specifically, the prevailing misconception, and consequent misuse, of the IMP, is addressed and clarified, both analytically and with a corresponding detailed numerical appraisal. In particular, throughout the paper, we demonstrate that any deterministic internal model characterising the wave excitation will be, by definition, an approximation, so the effectiveness of wave excitation estimation schemes does not derive directly from the adopted model, but depends on the bandwidth achieved within the chosen estimation strategy. Following these lines, we show that a simpler internal model can provide, overall, better results than more complex IMP structures. In particular, when referring to the two main models adopted in the literature, *i.e.*, harmonic oscillator

and random walk, the latter introduces just an additional state to the overall augmented system, while the former requires the inclusion of $2n_e$ modes, with n_e representing the number of harmonic components considered for the representation of the excitation force. Thus, the presented study establishes foundational principles to ensure a certain level of performance under general assumptions. In emphasising the nature of this study, it is important to mention that the objective is not to conduct a comparative analysis between different estimator structures, nor to conduct a robustness assessment or robust design. Rather, the convergence and performance characteristics of these structures are analysed individually, under diverse scenarios. Nevertheless, it is worth noting that certain commonalities and distinctions between the considered estimation structures, as candidates of the family of IMP-based estimators, are explored to derive general insights.

The subsequent sections of this paper are structured as follows. A review of fundamental WEC modelling principles and basics of estimations are given in Section 2. Section 3 delves into the introduction of Luenberger-based estimation approaches. In Section 4, a comprehensive discussion that illuminates the theoretical and practical implications associated with considering the wave excitation force model is given. To substantiate and validate our earlier findings and discussions, a series of general simulations are given in Section 5, considering both regular and irregular waves. Finally, Section 6 serves as the conclusion of this study, encapsulating the pivotal discoveries and delving into the ramifications of the proposed approach.

Notation

$Z(\omega)$, $z(t)$ denotes a Fourier transform pair. $\mathbb{Re}\{\cdot\}$ and $\mathbb{Im}\{\cdot\}$ denote the *real-part* and *imaginary-part* operators. $\mathbb{Re}\{\cdot\}$ and $\mathbb{Im}\{\cdot\}$ denote the *real-part* and *imaginary-part* operators, respectively. $\mathbb{R}_{>0}$ and $\mathbb{R}_{<0}$ represent the sets of positive and negative real numbers, respectively, while, $\mathbb{C}_{>0}$ and $\mathbb{C}_{<0}$ denote the sets of complex numbers with positive and negative real parts, respectively. s indicates the Laplace variable, for the Laplace domain. The symbol $\bigoplus$ denotes the direct sum of n matrices, *i.e.* $\bigoplus_{i=1}^{n} A_i = \text{diag}\{A_1, A_2, \ldots, A_n\}$. $z(t)$, and $v(t) = \dot{z}(t)$ denote the position, and velocity of the floating body, respectively. $f_e(t)$ and $u(t)$ denote the excitation and control forces, respectively. The convolution operator is denoted with the symbol $*$. The set of eigenvalues is obtained with the operator $\lambda\{\cdot\}$.

2. Preliminaries: WEC modelling

We present, within this section, a brief recall of the fundamentals underlying linear WEC modelling, as per the standard assumptions adopted within virtually all the literature in wave excitation force estimation and control (see Ringwood et al. (2014)). The hypotheses adopted are consistent with linear potential flow theory (Falnes, 2002), in which the motion associated with the WEC system, in a single-degree-of-freedom (DoF),[2] can be expressed in terms of the following differential equation,[3]

$$\ddot{z} = \mathcal{M}\left(f_e - f_r - f_h - u\right), \tag{1}$$

in which $z \in \mathbb{R}$ denotes the displacement of the WEC system in the DoF under analysis, $f_e(t) \in \mathbb{R}$ denotes the wave excitation force (*i.e.* the force exerted on the wetted surface of the device due to the incoming wave field), $f_h(t) \in \mathbb{R}$ is the hydrostatic restoring force, and $f_r(t) \in \mathbb{R}$ denotes the so-called radiation force, describing the fluid memory effects on the device response. The function u, with $u(t) \in \mathbb{R}$, denotes the control force, applied via an associated power take-off (PTO) system, to optimise the WEC performance (see *e.g.* (Ringwood

---

[2] The extension to the multi-DoF case can be pursued straightforwardly, by following standard arguments from potential flow theory (see Folley (2016)).

[3] From now on, the dependence on t is omitted when clear from the context.

et al., 2014)). Finally, the inverse generalised mass in Eq. (1) is defined as $\mathcal{M} = (m + \mu_\infty)^{-1}$, where μ_∞ is the so-called radiation added-mass at infinite frequency (see Falnes (2002)).

Within linear potential flow, the hydrostatic force can be computed as a linear map in z, *i.e.*

$$f_{\mathrm{h}} = k_{\mathrm{h}} z, \tag{2}$$

where $k_{\mathrm{h}} \in \mathbb{R}^+$ denotes the so-called hydrostatic stiffness. Radiation effects are modelled following the well-known Cummins' formulation (Cummins, 1962), in which f_{r} is computed in terms of a corresponding convolution operation

$$f_{\mathrm{r}} = k_{\mathrm{r}} * v, \tag{3}$$

in which $v = \dot{z}$ denotes the velocity of the associated DoF, and $k_{\mathrm{r}} \in L^2(\mathbb{R})$ is the radiation impulse response function, characterising the underlying radiation subsystem. The characterisation of the map k_{r} is performed in terms of numerical techniques, based on so-called boundary element methods (BEMs). In particular, BEM-based software packages, such as *e.g.* NEMOH (LHEEA, 2017), provide a finite set of data points (either in the time- or frequency-domain) describing the map k_{r}. As per standard practice within simulation, estimation, and control of WEC systems, and given the non-parametric nature of the output provided by BEM codes, the operation in (3) is approximated in terms of the output of a v-dimensional linear time-invariant, internally stable and strictly proper representation, *i.e.*

$$\dot{\theta} = F\theta + Gv,$$
$$f_{\mathrm{r}} \approx H\theta, \tag{4}$$

in which the triple $(F, G, H^{\mathsf{T}}) \in \mathbb{R}^{v \times v} \times \mathbb{R}^v \times \mathbb{R}^v$ can be computed via tailored system identification procedures (see *e.g.* (Peña-Sanchez et al., 2019a)).

Leveraging the representation in Eq. (4), Eq. (1) can be fully written in terms of a state–space system as

$$\dot{x} = Ax + B\left(f_{\mathrm{e}} - u\right)$$
$$y = Cx = z, \tag{5}$$

with a state-vector $x = [z \; v \; \theta]^{\mathsf{T}}$, $x(t) \in \mathbb{R}^n$, $n = 2 + v$, and where the matrices (A, B, C) are defined as

$$A = \begin{bmatrix} A_0 & B_0 H \\ GC_0 & F \end{bmatrix}, \quad B = \begin{bmatrix} B_0 \\ \mathbf{0} \end{bmatrix}, \quad C = \begin{bmatrix} C_0 & \mathbf{0} \end{bmatrix}, \tag{6}$$

with

$$A_0 = \begin{bmatrix} \mathbf{0} & 1 \\ -\mathcal{M}k_{\mathrm{h}} & \mathbf{0} \end{bmatrix}, \quad B_0 = \begin{bmatrix} \mathbf{0} \\ \mathcal{M} \end{bmatrix}, \quad C_0 = \begin{bmatrix} 1 & \mathbf{0} \end{bmatrix}, \tag{7}$$

where the $\mathbf{0}$ (null) matrices have appropriate dimensions.

3. Estimation frameworks for wave excitation

As highlighted in Section 1, numerous strategies have been proposed for the estimation of wave excitation force or torque. It is noteworthy that a substantial portion of these strategies rely on IMP theory, assuming an implicit deterministic model that characterises an unknown input to be estimated. In the context of this study, the focus is on the estimation of the wave excitation force. By way of example, the well-established Kalman estimation theory for unknown inputs, employing an infinite estimation horizon, can be placed within an IMP framework. In particular, Kalman-based estimators have found effective application in wave excitation force estimation, as presented in, for example, Nguyen and Tona (2018) or Davis and Fabien (2020), where the considered estimation schemes are coupled with random walk signal structures. The literature has also explored the convergence of Kalman-based estimators, as in Krener (2003), Rhudy and Gu (2013), providing a comprehensive understanding, from a general perspective. However, it is essential to note that this study operates within a deterministic framework. Consequently, convergence conditions within the context

of Kalman-based estimators, such as those relative to the covariance matrix, remain constant. For this particular study, as discussed in Section 1, two estimation structures are considered, being the most widespread and widely used estimation approaches in WEC systems. In steady-state conditions, the underlying estimation structure is essentially a Luenberger observer, *i.e.* it follows the approach described in Section 3.1, via Eq (8). This is discussed in detail within this section.

The techniques explored within the literature of wave excitation estimation for WECs, which are those effectively discussed within this paper, exploit the IMP (Francis and Wonham, 1976). To be precise, an implicit description of the wave excitation force is sought, based on a set of differential equations.

The underlying idea is that of providing an estimate $\tilde{f}_{\mathrm{e}}$ of the wave excitation force f_{e} based on available measurements for a given WEC system and the chosen implicit form to describe the excitation dynamics, in the spirit of the state estimation case presented in Section 3.1. In particular, the error between the estimated and measured motion of a WEC, denoted $e(t)$, is minimised to yield an (ideally) accurate estimate of f_{e}, assuming that the WEC model effectively reflects the actual system. As a matter of fact, the accuracy of the obtained $\tilde{f}_{\mathrm{e}}$ will rely heavily on, initially, how accurately the model represents the actual device behaviour, being hence able to '*decouple*' internal dynamics of the WEC system from the external force f_{e}.

3.1. State estimation

Within this section, we provide an overview of the fundamentals of standard state estimation, which are then used and extended accordingly for the case of wave excitation (*i.e.* unknown-input) estimation, in Section 3. In particular, leveraging the state–space representation of Eq (5), we discuss a standard method to compute an estimate $\tilde{x}$ of the state-vector x, based only on the available measures of the system. To provide a simplified account, as preparation for the results presented in the upcoming sections, we initially assume the WEC is in undisturbed conditions, *i.e.* $f_{\mathrm{e}} = 0$, $\forall t \in \mathbb{R}_{>0}$. In this case, we resort to the so-called Luenberger observer structure (Luenberger, 1964), *i.e.*

$$\dot{\tilde{x}} = A\tilde{x} - Bu + L(y - \tilde{y})$$
$$\tilde{y} = C\tilde{x} = \tilde{v}, \tag{8}$$

where the matrix L is the so-called observer gain, which essentially introduces a correction component proportional to the estimation error $y - \tilde{y}$.

Defining the estimation error as $e = x - \tilde{x}$, together with the WEC system description in Eq. (5) and associated observer in Eq. (8), the objective is that of designing the observer gain L such that $e \to 0$ as $t \to \infty$. With some algebraic manipulation, the following dynamical description for e can be achieved straightforwardly:

$$\dot{e} = (A - LC)e, \tag{9}$$

from which the associated trajectories, for any given observer initial condition $e(0)$, can be computed simply as

$$e(t) = \mathrm{e}^{(A - LC)t} e(0). \tag{10}$$

In simpler terms, ensuring that the observer gain L is designed such that $\lambda\{A - LC\} \subset \mathbb{C}_{<0}$, the set of complex numbers with negative real part, where $\lambda\{\cdot\}$ denotes the set of eigenvalues, and by the conditions outlined in, for example, Chen (1999), leads to the decay of the matrix exponential in Eq. (10) as $t \to \infty$. This decay guarantees the convergence of the state estimate, denoted as $\tilde{x} \to x$, regardless of the initial conditions of the observer. Various methods, such as those based on the Lyapunov equation, Ackermann's equation, or the Bass–Gura formulation (Chen, 1999), can be considered for the design of L, based on user-defined closed-loop dynamics for the estimator.
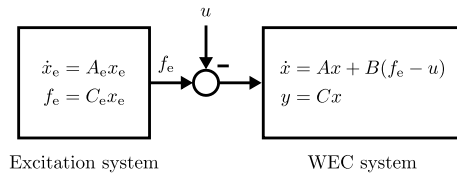
Fig. 1. Interconnection between the implicit form description used to describe the wave excitation process and the WEC dynamical system.

3.2. Implicit form description of the wave excitation

The family of observers analysed within this study represents the wave excitation force in terms of a linear deterministic model. In particular, the wave excitation force f_e is modelled in terms of an autonomous linear system driven by initial conditions, *i.e.* an implicit form description, as follows

$$\begin{cases} \dot{x}_e &= A_e x_e, \\ f_e &= C_e x_e, \end{cases} \tag{11}$$

with initial condition $x_e(0)$ and where the pair (A_e, C_e) is observable (see Goodwin et al. (2001)), and $A_e \in \mathbb{R}^{n_e \times n_e}$ and $C_e \in \mathbb{R}^{n_e}$. A schematic representation of the interconnection between the WEC and Eq (11) can be appreciated from Fig. 1.

The implicit form in Eq. (11) can represent a variety of deterministic signals. We show this by means of the following example dynamics:

$$\begin{aligned} \text{(I)} \ A_e &= \begin{bmatrix} 0 & 1 \\ 0 & 0 \end{bmatrix} &\rightarrow x_e(t) &= \begin{bmatrix} 1 & t \\ 0 & 1 \end{bmatrix} x_e(0), \\ \text{(II)} \ A_e &= \beta &\rightarrow x_e(t) &= e^{\beta t} x_e(0), \\ \text{(III)} \ A_e &= \begin{bmatrix} 0 & -\beta \\ \beta & 0 \end{bmatrix} &\rightarrow x_e(t) &= \begin{bmatrix} \cos(\beta t) & -\sin(\beta t) \\ \sin(\beta t) & \cos(\beta t) \end{bmatrix} x_e(0), \end{aligned} \tag{12}$$

where β is assumed to be a real constant for all three cases. Considering suitable initial conditions (according to the context), the equations in (13) define associated function spaces to describe the wave excitation signal, *i.e.*

$$\begin{aligned} \text{(I)} \quad & f_e \in \text{span}(\{1, t\}), \\ \text{(II)} \quad & f_e \in \text{span}(e^{\alpha t}), \\ \text{(III)} \quad & f_e \in \text{span}(\{\cos(\alpha t), \sin(\alpha t)\}). \end{aligned} \tag{13}$$

Notice that (I) generates polynomial functions, which are, by their nature, unbounded. (II), instead, describes exponential behaviour, which can be either asymptotically stable ($\alpha < 0$), constant – yet bounded – ($\alpha = 0$), or unstable ($\alpha > 0$).

To analyse the general case, suppose $\lambda \in \mathbb{C}$ is an eigenvalue of A_e, and let q be the dimension of its largest associated generalised eigenspace. The implicit form (11) is inherently able to generate the family of functions $\{t^i e^{\lambda t}\}_{i=0}^{q-1}$. Though effectively able to provide a wide variety of function spaces for the description of f_e, we know, from physical principles, that wave excitation is both a bounded and persistently exciting signal, meaning that only a subset of scenarios is representative: The eigenvalues of A_e must be simple, and can be either zero (*i.e.* an integrator) or complex conjugate pairs with zero real part. The former, which corresponds with case (II) in (13) with $\alpha = 0$, generates the space span(1). The latter, which can be associated with case (III) in (13), generates a space populated by trigonometric polynomials with frequencies directly linked with each pair of purely complex eigenvalues in $\lambda(A_e)$. Any other scenario (apart from the two described immediately above), leads to deterministic models which are either asymptotically stable, meaning that f_e tends to zero (hence violating the persistence of excitation condition) or unstable, meaning that f_e grows indefinitely, violating the bounded condition for the wave excitation. These two cases, referred to in the literature of WEC estimation as 'random walk' and 'harmonic oscillator' models, respectively, are the fundamental internal model building blocks for wave excitation, and are described in detail within the following paragraphs.

3.2.1. Random walk scheme

Following the discussion provided immediately above, for the random walk scheme, the matrices A_e and C_e are simply defined as,

$$A_e = 0, \quad C_e = \alpha. \tag{14}$$

Note that this effectively coincides with (II) in (13) with $\beta = 0$. Within this formulation, assuming reachability of the pair $(A_e, x_a(0))$, the excitation force, is modelled as a (locally) piecewise constant value, *i.e.*

$$f_e \in \text{span}(1). \tag{15}$$

Alternatively, the family of functions associated with the implicit form (14) can be characterised in terms of the so-called generating polynomial (Goodwin et al., 2001) as

$$\Gamma(s) = s, \tag{16}$$

with $s \in \mathbb{C}$. The root of this polynomial is, clearly, $s = 0$, which coincides with $\lambda(A_e)$. The value for $\alpha \in \mathbb{R}/0$ in C_e is used as in the case of the harmonic oscillator (see Eq. (14)).

3.2.2. Harmonic oscillator scheme

For this case, the excitation force is assumed to be defined in terms of the superposition of n_e sinusoidal modes (polychromatic process). Consequently, the matrices A_e and C_e can be defined, without any loss of generality, as follows:

$$A_e = \bigoplus_{p=1}^{n_e/2} \begin{bmatrix} 0 & \omega_p \\ -\omega_p & 0 \end{bmatrix}, \quad C_e = \begin{bmatrix} \mathbf{1}_{n_e} \otimes \begin{bmatrix} \alpha & 0 \end{bmatrix} \end{bmatrix}, \tag{17}$$

featuring a set of 'natural' frequencies $\mathcal{W}_p = \{\omega_p\}_{p \in \mathbb{N}_{n_e}}$, with $\omega_p \in \mathbb{R}_{>0}$, of the considered harmonic oscillator to represent the excitation force, and $\mathbf{1}_{n_e} \in \mathbb{R}^{n_e}$ a vector with all its entries equal to one. Although the value for $\alpha \in \mathbb{R}$ in C_e is often used as a design parameter, for the convergence analysis presented within this paper, it can be set to $\alpha = 1$ without any loss of generality. Note that it is straightforward to see that, with the choice of matrices in Eq. (17), the excitation force is essentially modelled as a finite sum of trigonometric polynomials, *i.e.*

$$f_e \in \text{span}(\{\cos(\omega_p t), \sin(\omega_p t)\}_{p \in \mathbb{N}_{n_e/2}}). \tag{18}$$

Analogously to the random walk case, presented in Section 3.2.1, the implicit from described via (17) can be alternatively written in terms of an associated generating polynomial as:

$$\Gamma(s) = \prod_{p=1}^{n_e/2} (s^2 + w_p^2). \tag{19}$$

The roots of this polynomial, which indeed coincide with $\lambda(A_e)$, with A_e as in (17), are given by the set $\pm \omega_p J$, where p ranges from 1 to $n_e/2$.

3.3. Estimation

It is possible to devise a joint state and input estimator following the Luenberger structure detailed in Section 3.1, specifically in Eq. (8) (Luenberger, 1964), as shown in Fig. 2. In particular, by combining the state–space representations for the WEC system in Eq. (5) and excitation force process in Eq. (11), an 'augmented' system can be obtained, as follows:

$$\begin{cases} \dot{x}_a &= A_a x_a + B_a u \\ y &= C_{az} x_a, \end{cases} \tag{20}$$

where $x_a = \begin{bmatrix} x & x_e \end{bmatrix}^\top$, $y = z$, and the set of matrices in Eq. (20) are defined as

$$A_a = \begin{bmatrix} A & BC_e \\ \mathbf{0} & A_e \end{bmatrix}, \quad B_a = \begin{bmatrix} -B \\ \mathbf{0} \end{bmatrix} \quad C_{az} = \begin{bmatrix} C & \mathbf{0} \end{bmatrix}. \tag{21}$$

Note that, using the implicit form description chosen for the wave excitation force, as per Eq. (11), estimation of the augmented state
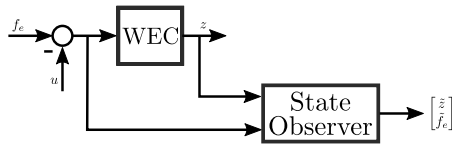
Fig. 2. A general estimation scheme in WEC systems is presented, using a state observer.

vector in Eq. (25), denoted as $\tilde{x}_a$, can be effectively used to provide an estimate $\tilde{f}_e$ accordingly, i.e.

$$\tilde{f}_e = C_{af}\tilde{x}_a, \quad \text{where} \quad C_{af} = \begin{bmatrix} 0 & C_e \end{bmatrix}, \tag{22}$$

so that the problem now reduces to computing $\tilde{x}_a$ based on the available measures of the WEC system (position z, in this case). Then, the system comprising y and f_e (or analogously $\tilde{f}_e$) is given by A_a, B_a and C_a, with

$$C_a = \begin{bmatrix} C_{af} \\ C_{az} \end{bmatrix}. \tag{23}$$

Following the state estimation case outlined in Section 3.1, an estimator structure can be presented as follows:

$$\dot{\tilde{x}}_a = A_a\tilde{x}_a + B_au + L(y - \tilde{y}), \tag{24}$$

where, analogously to the case presented in Eq. (8), the observer gain L needs to be chosen such that $\lambda\{A_a - LC_a\} \subset \mathbb{C}_{<0}$ to guarantee convergence, *i.e.* $e \to 0$, under the chosen implicit form description for the wave excitation.

4. Analytical investigation

This section delves into the analytical core, introducing key results that solidify the central arguments given in this study. It is noteworthy to mention that although, in Fig. 2, a control force $u(t)$ is schematically shown for completeness, for presenting a general estimator analysis it can be removed, as it is a known quantity. The outcome elucidated in Section 3 yield the following closed-loop estimation augmented system, that encompass both the WEC and the estimator dynamics, as follows:

$$\begin{cases} \dot{\tilde{x}}_a = (A_a - LC_a)\tilde{x}_a + \begin{bmatrix} L & B \end{bmatrix}\begin{bmatrix} z \\ u \end{bmatrix} \\ \tilde{f}_e = \begin{bmatrix} 0 & C_e \end{bmatrix}\tilde{x}_a = C_{af}\tilde{x}_a \\ \tilde{z} = \begin{bmatrix} C & 0 \end{bmatrix}\tilde{x}_a = C_{az}\tilde{x}_a \end{cases} \tag{25}$$

It is worth mentioning that, for the sake of completeness, the control force $u(t)$ is included in Eq. (25), but can be safely assumed to be null (*i.e.* zero) without any loss of generality. Consequently, Eq. (25) defines an observer structure for estimating $\tilde{x}_a$, in particular, the WEC motion, indicated as $z(t)$, and the unknown excitation force, $\tilde{f}_e$. The resulting block diagram for motion and excitation force estimation is depicted in Fig. 3, using a time-domain block representation, including the WEC dynamics and the observer (estimation) scheme, assuming null control force u.

Based on the closed-loop observer expression in Eq (25), and with the objective of establishing analytical conditions for excitation force estimation effectiveness, the following system can be formulated:

$$\begin{cases} \begin{bmatrix} \dot{\hat{x}}_a \\ \dot{x} \end{bmatrix} = \begin{bmatrix} A_a - LC_a & LC \\ 0 & A \end{bmatrix}\begin{bmatrix} \hat{x}_a \\ x \end{bmatrix} + \begin{bmatrix} 0 \\ B \end{bmatrix}f_e, \\ \tilde{f}_e = \begin{bmatrix} C_{af} & 0 \end{bmatrix}\begin{bmatrix} \hat{x}_a \\ x \end{bmatrix}. \end{cases} \tag{26}$$

This system combines excitation force estimation and WEC models, facilitating the mapping from f_e (actual excitation force) to $\tilde{f}_e$ (estimated excitation force) for the assessment of $\tilde{f}_e$ estimation effectiveness. It is

important to note that, even though f_e is an inaccessible and unmeasurable quantity, assuming full knowledge of f_e, as in Eq. (26), allows general conditions to be given for effective estimation of excitation force, following standard results in IMP theory.

4.1. Frequency domain

Following Fig. 3, the augmented structure depicted in Eq. (26) can be equivalently defined in the frequency domain, as illustrated in Fig. 4. Assuming a WEC system in the state–space domain represented by:

$$G_o(s) \equiv \left[\begin{array}{c|c} A & B \\ \hline C & 0 \end{array}\right]. \tag{27}$$

the resulting estimation structures, $z \to \tilde{f}_e$ and $z \to \tilde{z}$, can be defined in terms of the dynamic structures G_z and G_f. These structures are derived from the estimation scheme depicted in Fig. 3 and Eq. (26), as follows:

$$G_z(s) \equiv \left[\begin{array}{c|c} A_a & L \\ \hline C_{az} & 0 \end{array}\right], \quad G_f(s) \equiv \left[\begin{array}{c|c} A_a & L \\ \hline C_{af} & 0 \end{array}\right]. \tag{28}$$

Thus, the resulting closed-loop estimation schemes ($z \to \tilde{f}_e$ and $z \to \tilde{z}$), as illustrated in Figs. 3 and 4, can be expressed as transfer functions, as follows:

$$z \mapsto \tilde{z} \equiv (I + G_z)^{-1} G_z, \tag{29}$$

$$z \mapsto \tilde{f}_e \equiv (I + G_z)^{-1} G_f, \tag{30}$$

while the final force-to-force structure (see Fig. 3), required for estimator performance study and assessment, is given by:

$$f_e \mapsto \tilde{f}_e \equiv (I + G_z)^{-1} G_f G_o. \tag{31}$$

Similarly, the mappings in Eq. (28) can be explicitly defined, in the frequency domain, as follows:

$$G_f(s) = \begin{bmatrix} C_e & 0 \end{bmatrix}\Psi(s)^{-1}L,$$
$$G_z(s) = \begin{bmatrix} 0 & C \end{bmatrix}\Psi(s)^{-1}L, \tag{32}$$

with

$$\Psi(s) = \begin{bmatrix} (sI - A) & -BC_e \\ 0 & (sI - A_e) \end{bmatrix}, \tag{33}$$

and, for the sake of simplifying the notation, the nominal WEC model can be expressed as:

$$G_o(s) = C(sI - A)^{-1}B. \tag{34}$$

Thus, using the upper diagonal nature of $\Psi(s)$, in Eq. (33), its inverse can be computed as

$$\Psi(s)^{-1} = \begin{bmatrix} (sI - A)^{-1} & (sI - A)^{-1}BC_e(sI - A_e)^{-1} \\ 0 & (sI - A_e)^{-1} \end{bmatrix}. \tag{35}$$

By combining the expressions in Eq. (32), with Eq. (35), then,

$$G_f(s) = C_e (sI - A_e)^{-1} L_e. \tag{36}$$

and

$$G_z(s) =$$
$$C (sI - A)^{-1} L_o + C (sI - A)^{-1} BC_e (sI - A_e)^{-1} L_e. \tag{37}$$

with

$$L = \begin{bmatrix} L_o \\ L_e \end{bmatrix}, \quad L_o \in \mathbb{R}^n, \quad \text{and} \quad L_e \in \mathbb{R}^{n_e}. \tag{38}$$
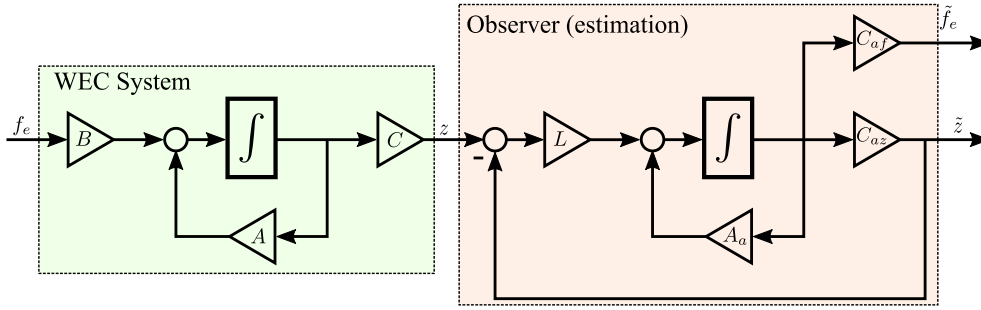
Fig. 3. General time-domain estimation scheme in WEC systems. In particular, the motion (position) and an unknown excitation force are estimated.
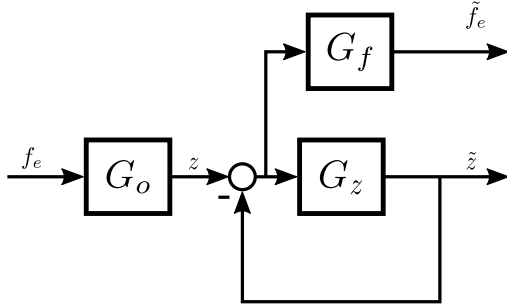

Fig. 4. Frequency domain resulting estimation scheme.

4.2. Convergence analysis of estimation errors

The sets of eigenvalues corresponding to A and A_e are defined as:

$$\Lambda_o \equiv \lambda\{A\}, \quad \Lambda_e \equiv \lambda\{A_e\} \in \mathbb{C}^{n_e}, \tag{39}$$

with $\Lambda_o \in \mathbb{C}^n$ and $\Lambda_e \in \mathbb{C}^{n_e}$. Specifically, owing to the inherent stability characteristic of WEC systems, it holds that $\forall \lambda_i \in \Lambda_o$, then $\lambda_i \in \mathbb{C}_{<0}$, where $i = 1, \dots, n_e$. Similarly, considering the previously discussed harmonic oscillator and random walk estimation schemes (see Section 3.2), $\forall \lambda_i \in \Lambda_e$, then $\mathbb{Re}\{\lambda_i\} = 0$, with $i = 1, \dots, n_e$, or $\lambda_i = j\omega_p$, or $\lambda_i = j\omega_p$, with $p = 1, \dots, n_e$, always forming complex conjugate pairs. It is noteworthy that the set of eigenvalues Λ_e is determined by the roots of the generating polynomials $\Gamma(s)$ in Eqs. (15) and (19).

Hence, each mapping in Eqs. (32) to (37), namely $G_o(s)$, $G_f(s)$, and $G_z(s)$, can be articulated as transfer functions, delineated in terms of denominator and numerator factors (polynomials). Thus, the WEC model is represented by the transfer function:

$$G_o(s) = C(sI - A)^{-1}B = D_o(s)^{-1}N_o(s), \tag{40}$$

where $D_o(s)$ and $N_o(s)$ denote the denominator and numerator factors of $G_o(s)$, respectively. In particular,

$$D_o(s) = \prod_{i=1}^{n}(s - \lambda_i), \quad \lambda_i \in \Lambda_o. \tag{41}$$

Similarly,

$$G_f(s) = C_e(sI - A_e)^{-1}L_e = D_e(s)^{-1}N_e(s), \tag{42}$$

with

$$D_e(s) = \prod_{i=1}^{n_e}(s - \lambda_i), \quad \lambda_i \in \Lambda_e. \tag{43}$$

Analogously

$$G_z(s) =$$
$$C(sI - A)^{-1}L_o + C(sI - A)^{-1}BC_e(sI - A_e)^{-1}L_e =$$
$$D_o(s)^{-1}N_{L_o}(s) + D_o(s)^{-1}N_o(s)D_e(s)^{-1}N_e(s). \tag{44}$$

where $N_{L_o}(s)$ denotes a generic numerator factor associated with L_o, which cannot be defined in general, even though its specific definition does not impact the presented analysis. Thus, following the relationships schematically depicted in Fig. 4, the resulting estimator mappings can be expressed in terms of the estimation error,

$$z \mapsto e = z - \tilde{z} \equiv \Big(D_o(s)D_e(s) + D_e(s)N_{L_o}(s) +$$
$$N_o(s)N_e(s)\Big)^{-1}D_o(s)D_e(s). \tag{45}$$

Based on Eqs. (32), (34), and (45), the resulting $f_e \to \tilde{f}_e$ mapping can be expressed in terms of its numerator and denominator factors, as follows

$$f_e \mapsto \tilde{f}_e \equiv$$
$$D_o(s)^{-1}N_o(s)D_e(s)^{-1}N_e(s)\Big(D_o(s)D_e(s) + D_e(s)N_{L_o}(s) +$$
$$N_o(s)N_e(s)\Big)^{-1}D_o(s)D_e(s) =$$
$$N_o(s)N_e(s)\Big(D_o(s)D_e(s) + D_e(s)N_{L_o}(s) +$$
$$N_o(s)N_e(s)\Big)^{-1} \tag{46}$$

Analysis of Eq. (46) reveals that when evaluating $f_e \mapsto \tilde{f}e$ within the set of eigenvalues Λ_e, as prescribed by the IMP, *i.e.* $D_e(\lambda_i) = 0$, $\forall \lambda_i \in \Lambda_e$ (see Eq. (42)), the resulting mapping is equal to the identity mapping, specifically:

$$f_e \mapsto \tilde{f}e \overset{s \in \Lambda e}{=} 1, \tag{47}$$

which is equivalent to:

$$z \mapsto e \overset{s \in \Lambda e}{=} 0. \tag{48}$$

4.3. Analysis

The frequency-domain result in Eq. (46) shows the consistency of the mapping $f_e \mapsto \tilde{f}_e$ with IMP theory. IMP theory suggests that, when the natural modes of the excitation signal f_e, in the generating polynomials $\Gamma(s)$ in Eqs. (15) and (19), for the harmonic oscillator and random walk, respectively, are encompassed within Λ_e, zero tracking error (estimation within the framework of estimation theory) can be assured in steady state. Consequently, as shown in the forthcoming simulation/experimental results in Section 5, it becomes feasible to achieve zero estimation or tracking error in steady state, when dealing with combinations of purely sinusoidal signals. This is accomplished when employing the harmonic oscillator, which incorporates purely imaginary eigenvalues (lying on the imaginary axis).

Similarly, zero tracking or estimation error in the steady state is guaranteed for step-type signals when the integrator model (characterised by a pole at the origin) is employed to define Λ_e, representing the random walk scheme. The inclusion of a harmonic oscillator or random walk model within the definition of Λ_e does not automatically ensure convergence, as convergence will depend on the alignment between the inclusion of the appropriate spectral components, as per IMP theory, and the spectral definition, or generating polynomial, $\Gamma(s)$, of

the excitation force. Conversely, when defining a Λ_e with large dimension structure, numerical errors can be introduced due to heightened computational complexity (poor numerical condition). Consequently, given the stochastic and irregular nature of realistic ocean waves (absence of a generating polynomial), the effectiveness, or ineffectiveness, of an estimator is predominantly governed by the resulting closed-loop bandwidth of the estimation structure. This bandwidth is determined by the placement of the closed-loop eigenvalues, resulting from the fusion of the WEC model and the state observer. In mathematical terms, the closed-loop bandwidth hinges on the eigenvalues of the closed-loop matrix:

$$\Lambda_{CL} \equiv \lambda \left\{ A_a - LC_a \right\}. \tag{49}$$

Hence, as the estimation convergence is dictated by Λ_{CL}, the convergence velocity of the estimator is characterised by the minimum $|\lambda^\star|$, with $\lambda^\star \in \Lambda_{CL}$. However, the pursuit of a greater $|\lambda^\star|$, to speed up the convergence, can generate numerical inaccuracies and problems, attributed to the burden of high computational demands, generated by large numbers. Therefore, a discernible trade-off materialises between convergence effectiveness and computational feasibility.

It must be noted that the resulting bandwidth of the estimator structure (see Fig. 3), is given by

$$\text{Bandwidth} \propto \min \left(\left| \mathbb{Re} \left\{ \lambda^\star \right\} \right| \right), \text{ with } \lambda^\star \in \Lambda_{CL}, \tag{50}$$

while the eigenvalue defining the closed-loop bandwidth is referred to as the dominant eigenvalue (or the *slowest eigenvalue*), as it governs the convergence velocity.

5. Case study

This section presents the outcomes derived from the implementation of the estimation methodologies outlined in Sections 3.2.1 and 3.2.2. The presented analysis is performed considering, as a nominal model, the linear time-invariant (LTI) system in García-Violini et al. (2024) derived from experimental tests, by the application of system identification routines (see García-Violini et al. (2024) for more details). Thus, the nominal model, referred to as $G_o(s)$ in the context of this study, is a stable and passive LTI system of fourth order. It is essential to note that the results presented in this study are insensitive to the specific choice of nominal model. However, as elaborated in subsequent discussion, the incorporation of a realistic experimental platform allows practical issues to be addressed, including hydrodynamic uncertainty, non-linearities, and effects exerted by the electromechanical components. Consequently, this enables an assessment of the estimation performance under authentic operating conditions.

The analysis, assessment, and results presented in this study are based on the experimental setup depicted in Fig. 5, presenting both a photograph and a schematic of the prototype system. The experimental infrastructure, extensively used in previous studies (Ferri et al., 2012; Nguyen et al., 2016; García-Violini et al., 2023; Faedo et al., 2023; García-Violini et al., 2024), incorporates a real-time software architecture implemented through the Matlab/Simulink Real-Time Toolbox (version 2016b) for data acquisition (The Mathworks Inc., 2024b). A detailed description of the experimental setup, encompassing the WEC prototype, sensing and actuation systems, hardware, computer and acquisition, and wave basin dimensions, can be found in, for example, (García-Violini et al., 2021, 2024). Notably, the prototype utilised in this study is based on the Wave Star WEC system (Hansen and Kramer, 2011), a well-established concept in the wave energy field. It is important to acknowledge that, within the context of this study, and given the rotational nature of the PTO assembly, the analysis in this section considers rotational motion rather than translational motion. Thus, for the definitions in Eq. (1), the forces are replaced by torques (f_e by τ_e), mass by inertia ($\mathcal{M}$ by $\mathcal{I}$), etc.
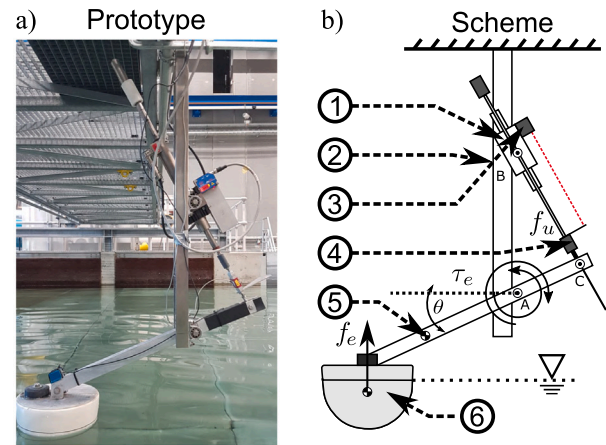

Fig. 5. The prototype system used for estimation assessment, considering the methodologies discussed in Sections 3.2.1 and 3.2.2. The setup, replicates the Wave Star WEC system. The references indicate: (1) the PTO system; (2) the mounting structure; (3) the motion sensor; (4) the load cell (for forces measurement); (5) the centre of gravity (CoG) of the whole structure; and (6) centre of gravity of the buoy.

5.1. Closed-loop eigenvalue placement for estimation

While there are numerous (infinite) configurations for placement and assignment of eigenvalues in closed-loop estimation, for the sake of a systematic and methodical approach, this study adopts the repeated assignment of poles at purely real locations. From the definition in Eq. (49), the assignment of poles to closed-loop estimation is structured, as follows:

$$\Lambda_{CL} \equiv \lambda \left\{ A_a - LC_a \right\} = \left\{ \lambda^\star, \dots, \lambda^\star \right\}, \tag{51}$$

with $\lambda^\star \in \mathbb{R}_{<0}$. Consequently, Ackermann's method is applied to determine the estimator gain L in each case, ensuring the desired set Λ_{CL} (Ackermann, 1972). Ackermann's method, for eigenvalue placement, is a control system design method for linear time-invariant systems. It assigns desired closed-loop eigenvalue locations using Ackermann's formula, which calculates the estimation gain L based on the controllability matrix of the pair $\left(A_a^\mathsf{T}, C_a^\mathsf{T} \right)$, with T denoting the transpose of a matrix. The method utilises the controllable canonical form for analytical computations. Various computation platforms have built-in routines for its implementation in practical control system design (The Mathworks Inc., 2024b).

It is crucial to emphasise that, despite an infinite number of combinations of closed-loop eigenvalue positions, this study practically encompasses all cases. The chosen methodology aims to illustrate the impact of closed-loop bandwidth (see Eqs. (49) and (50)) on estimator performance, giving prominence to the dominant eigenvalues, *i.e.* those with the smallest real part in magnitude (absolute value), as pivotal determinants in all scenarios. Moreover, the placement of closed-loop eigenvalues can be achieved, for instance, using alternative methods such as linear quadratic Gaussian (LQG) design, *i.e.* a Kalman-based filter with an infinite estimation horizon solving an algebraic Riccati equation, ultimately determining the location of these eigenvalues and providing a specific closed-loop bandwidth (Goodwin et al., 2001). For instance, LQG methods ensure minimum variance in a 2-norm sense, based on designated weighting matrices for the noise variance associated with the state vector and output. Similarly, closed-loop eigenvalue positions can be determined using alternative methods, such as those based on robust techniques (*e.g.* $\mathcal{H}_\infty$), computed for example with linear matrix inequalities (LMIs), or Riccati equations. However, each computational methodology, tailored to address specific design specifications, results in the definition of a distinct gain L and, consequently, a particular bandwidth. As shown later, this bandwidth
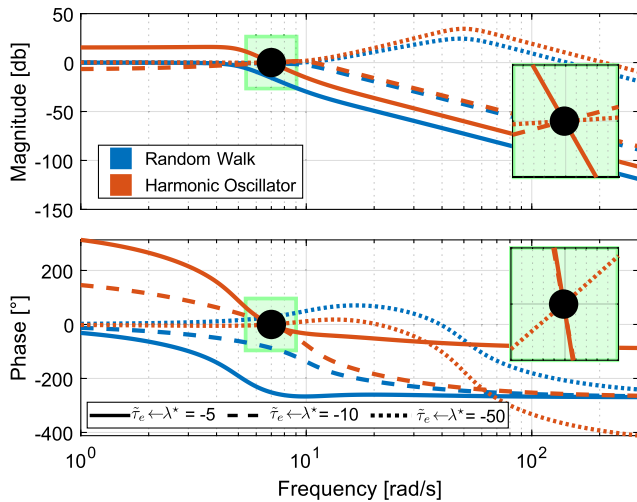
Fig. 6. Frequency response analysis for the mapping $\tau_e \rightarrow \tilde{\tau}_e$. The matching at $\omega_o = 7$ rad/s, achieved with the harmonic oscillator, is indicated with a solid-black dot.

Fig. 7. Spectral analysis of the excitation torque experienced by the prototype when excited with a monochromatic wave, revealing evident harmonic distortion.

emerges as the key driver influencing estimation performance. It is crucial to note that the outcomes of the presented study are not affected by the particular methodology considered for closed-loop eigenvalue value placement.

5.2. Assessment scenarios: Excitation torque signals

For this study, three categories of excitation torque signals are considered, which are used in three assessment scenarios.

5.2.1. Scenario 1: Ideal monochromatic wave
Excitation torque

Firstly, an ideal sinusoidal wave excitation torque (ideal monochromatic excitation torque), with angular frequency $\omega_o = 7$ rad/s, is used for estimator assessment:

$$\tau_e = \sin(7t). \tag{52}$$

This scenario enables a thorough analysis of the steady-state response.

Estimator

Focusing on an ideal (simulated) monochromatic wave with frequency $\omega_o = 7$ rad/s, the harmonic oscillator matrix A_e is defined as indicated in Eq. (17), with $\mathcal{W}_p = \{\omega_o\}$, *i.e.* an unique ω_p, ensuring a perfect alignment in the mapping from τ_e to $\tilde{\tau}_e$, particularly at ω_o ($\tau_e \rightarrow \tilde{\tau}_e|_{s=\pm j\omega_o} = 1$), as illustrated in Eq. (46). To design an estimator based on a random-walk scheme, the unknown excitation torque is modelled with $A_e = 0$, as indicated in Eq. (14).

The frequency response of the resulting closed-loop estimation mapping,*i.e.* from torque to estimated torque ($\tau_e \rightarrow \tilde{\tau}_e$), is defined for $\lambda^\star = -5, -10$, and -50 rad/s, are depicted in Fig. 6. Specifically, in Fig. 6, a close-up around $\omega_o = 7$ rad/s is presented within a shadowed green box to clearly illustrate the perfect matching at 7 rad/s, achieved with the harmonic oscillator. Without loss of generality, the choice of each $\lambda^\star$ is made for illustrative purposes, aiming to mitigate exaggerated time-domain responses, for simplified visualisation of the results (discussed in Section 5.3).

5.2.2. Scenario 2: Experimental monochromatic wave
Excitation torque

For the second and third assessment scenarios, experimentally acquired wave excitation torques are utilised (see, for example, Faedo et al. (2023)). Simultaneously, while the system is affected by the corresponding wave (regular and irregular waves for the second and
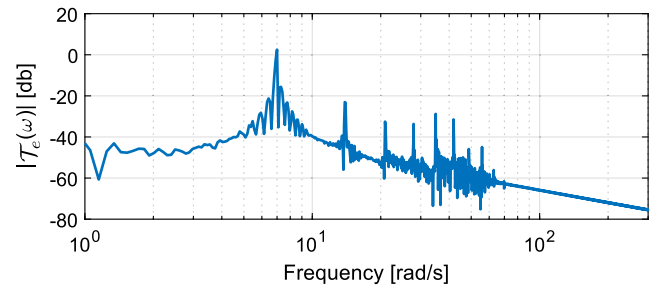
third scenarios, respectively), the wave excitation torque is acquired and used for estimation performance assessment. For a comprehensive discussion on the signal acquisition procedure, the interested reader is directed to García-Violini et al. (2024).

Specifically, for the second scenario, the prototype is exposed to a monochromatic wave with frequency $\omega_o = 7$ rad/s. Unlike the ideal case addressed in Scenario 1, harmonic distortion is present in the wave excitation torque for this experimental case (nonlinear effects), adding a layer of complexity to the estimation process. Fourier analysis of the magnitude of the wave excitation torque is depicted in Fig. 7. Thus, in Fig. 7, harmonic distortion can be detected, deviating from a purely sinusoidal waveform, with harmonics observed at 7 (fundamental component), 14, 21, ..., rad/s. The use of an experimental monochromatic excitation allows nonlinearity to be clearly identified, via harmonic production, and its effect on estimator performance can be clearly noted, isolated and analysed.

Estimator

In this scenario, the assessed estimation schemes are those designed for Scenario 1, where the corresponding frequency responses are illustrated in Fig. 6, using $\mathcal{W}_p = \{\omega_o\}$ for estimators based on the harmonic oscillator structure, and $A_e = 0$ for schemes grounded in the random walk structure, while the closed-loop estimation bandwidth is defined with $\lambda^\star = -5, -10$, and -50 rad/s, across all the examined estimation structures. The choice of each $\lambda^\star$ is made, without loss of generality, for illustrative purposes, aiming to deal with exaggerated time-domain responses (as discussed in Section 5.3).

5.2.3. Scenario 3: Irregular wave
Excitation torque

For the third scenario, an experimentally derived excitation torque, exerted when the prototype is exposed to a panchromatic wave, based on a JONSWAP spectrum (Hasselmann, 1973) with parameters $T_p = 1.836$ s ($\Omega_p = 3.42$ rad/s), $H_s = 0.1042$ m, and $\gamma = 3.3$ as typical period (peak frequency), significant wave height, and peak shape parameter, respectively, is employed. For this third case, the wave selection follows the details outlined in García-Violini et al. (2024), representing realistic (scaled) wave conditions in a full-scale version of the prototype.

A Fourier analysis for the magnitude of the wave excitation torque is shown in Fig. 8, where the spectral components used in a set of estimators based on the harmonic oscillator scheme, subsequently discussed in the following subsection, are indicated with solid-black dots.

In this scenario, similar to the experimental monochromatic case in Scenario 2, the fluid–structure interaction, imperfect *wavemaking*, and mechanical interaction in the PTO can introduce nonlinear behaviour and harmonic distortion. Furthermore, this scenario introduces additional complexity due to the broadband and dense nature of the excitation process, with the particular absence of separable harmonic behaviour.
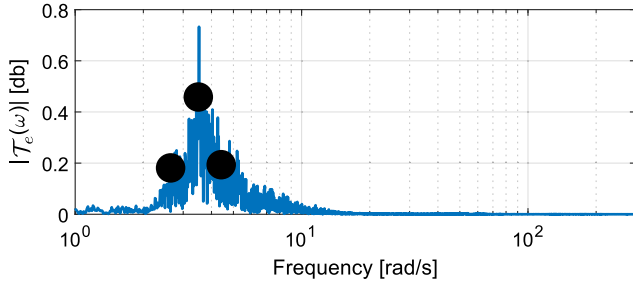
Fig. 8. Spectral analysis of the excitation torque experienced by the prototype when excited with a JONSWAP-based panchromatic wave. The spectral components considered in A_e for the harmonic oscillator are denoted with solid black dots.

Estimator

In this assessment scenario, a set of estimators based on a random walk scheme (using $A_e = 0$), and a set estimator based on a harmonic oscillator structure, are considered. For the set of estimators relying on the harmonic oscillator structure, a perturbation model A_e is introduced, defined with the following three spectral components:

$$\mathcal{W}_p \equiv \{0.75\Omega_p, \Omega_p, 1.25\Omega_p\}, \tag{53}$$

where $\Omega_p = 3.42$ rad/s denotes the peak frequency of the considered sea-state. The definition in Eq. (53) is designed to achieve a balance between numerical complexity and a tractable number of spectral components covering the excitation torque, avoiding potential numerical issues. However, increasing the number of spectral components in A_e intensifies the computational burden and introduces poor numerical conditioning. Hence, despite a wide range of possibilities for the number $n_e/2$ of spectral components ω_p, the chosen approach distinctly highlights the constraints of the harmonic oscillator. This is especially notable compared to the random walk scheme, which does not necessitate any additional model complexity. Thus, the presented definition of A_e, derived from Eq. (53), offers a good balance between spectral coverage and numerical complexity.

For this third scenario, the selected closed-loop eigenvalues are $\lambda^\star = -5, -10$, and -30 rad/s, which are chosen for illustrative purposes, avoiding extreme responses (as discussed in Section 5.3). It is essential to highlight that, unlike the first two scenarios involving monochromatic cases, in this scenario the fastest closed-loop eigenvalue is $\lambda^\star = -30$ rad/s whereas, in the monochromatic cases is $\lambda^\star = -50$ rad/s. This strategic choice is intended, without loss of generality, to mitigate extreme peak values and prevent extreme transients $\tilde{\tau}_e$.

Fig. 9 illustrates the frequency response of the mapping $\tau_e \to \tilde{\tau}_e$ for this third scenario. Black-solid dots, in Fig. 9, indicate the exact alignment of spectral components in the perturbation model A_e (refer to Eq. (53)), $\forall \lambda^\star \in \mathcal{W}_p$. These points, match the locations indicated with black dots in Fig. 8. The black dots in Figs. 8 and 9 emphasise the fulfilment of the matching condition, for the harmonic oscillator case, validating the analysis in Eq. (46). A critical observation, from Fig. 9, is the escalating amplification behaviour with the increase of the closed-loop bandwidth (by considering larger, or faster, closed-loop eigenvalues). This phenomenon leads to a progressive amplification in the estimator results.

5.3. Results

The time-domain results for the estimators based on random walk and harmonic oscillator perspectives are presented separately below. It is essential to highlight that in all the examined scenarios, encompassing simulations and experiments, the time extension is sufficient to ensure the attainment of a steady-state response.
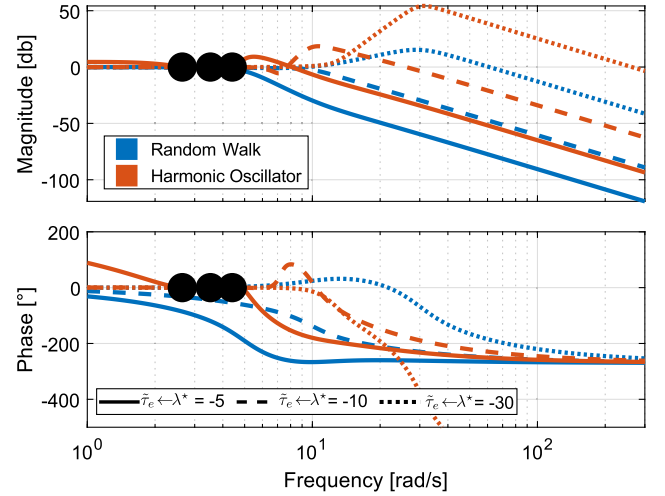

Fig. 9. Frequency response analysis for the mapping $\tau_e \to \tilde{\tau}_e$, considering three spectral components in the perturbation model (solid black dots).
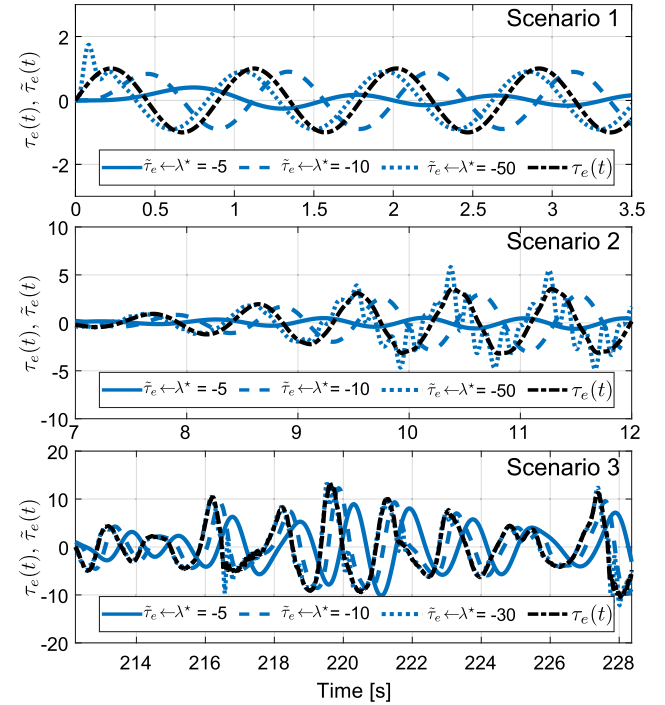

Fig. 10. Excitation torque estimates for the random walk in Scenarios 1 (top), 2 (middle), and 3 (bottom). Closed-loop eigenvalues $\lambda^\star = -5, -10$, and -50 are studied.

5.3.1. Random walk results

The time-domain results obtained with the presented estimation schemes based on random walk structures, for Scenarios 1, 2, and 3, are shown in this section. Thus, the time traces obtained for each scenario are shown in Fig. 10-top, -middle, and -bottom, respectively.

From the results for Scenario 1, in Fig. 10-top, it can be noted that the estimate does not converge to the actual excitation signal, regardless of the closed-loop eigenvalue locations. It must be noted that, irrespective of the value of $\lambda^\star$, a clear phase lag is prevalent, which is supported by the resulting estimator frequency response in Fig. 6. Thus, it is clear that the random walk cannot achieve adequate performance under these operation conditions. By extrapolating the findings from Fig. 6 for $|\lambda^\star| > 50$, the phase lag can be addressed

through an extension of the estimator bandwidth. Therefore, by adopting a broader bandwidth, specifically with $|\lambda^\star| > 50$, substantial mitigation of the phase lag becomes possible. Nonetheless, extending the bandwidth can lead to the emergence of additional amplification bands, as depicted in the case of $\lambda^\star = -50$ between 10 and 200 rad/s in Fig. 6. The increased amplification, while not impacting results in an ideal monochromatic scenario, where its power spectral density is fully contained in a single component. However, this amplification can pose a significant challenge in more realistic cases, with a distributed power spectral density, as discussed in Scenarios 2 and 3 below.

The time-domain results for Scenario 2 are shown in Fig. 10-middle. Similar to the results presented in Scenario 1, in Scenario 2 the estimators based on random walk schemes do not achieve perfect convergence to the actual excitation torque. Specifically, it is observable that while mitigation of the phase lag is evident in the comparison between $\lambda^\star = -10$ and $\lambda^\star = -50$, oscillatory behaviour becomes increasingly predominant. This behaviour arises from the interaction, in the frequency domain, between the spectral content of the excitation signal (see Fig. 7) and the frequency response of the different considered estimator structures (see Fig. 6). Therefore, when expanding the bandwidth to attain an estimator frequency response closer to unity, an increased amplification band is generated as a side effect. This amplification magnifies the spectral content of the excitation signal, detrimentally affecting the quality of the estimate. This impact is evident in the prevalent oscillations observed when $\lambda^\star = -50$.

The time-domain results for Scenario 3 are presented in Fig. 10-bottom. Notably, it is evident that the estimation schemes based on the random walk approach consistently deliver satisfactory performance across virtually all analysed cases ($\lambda^\star = -5, -10$, and -30). As previously discussed, and further explored in the subsequent section for the harmonic oscillator case, this behaviour is elucidated by examination of the spectral content of the excitation signal (refer to Fig. 7) and the amplification levels introduced by each estimation scheme (refer to Fig. 6). In this scenario, unlike the results for Scenario 2, the spectral content of the excitation signal is compensated by the frequency response of the estimation scheme leading to adequate performance.

5.3.2. Harmonic oscillators results

The time-domain results obtained with the presented estimation schemes based on harmonic oscillator structures, for Scenarios 1, 2, and 3, are shown in this section. Thus, the time traces obtained for Scenario 1, 2, and 3 are shown in Fig. 11-top, -middle, and -bottom, respectively.

The results for Scenario 1, in Fig. 11-top, emphasise the perfect convergence that can be achieved by this estimation scheme when assessing ideal regular waves (periodic with compact support), which is a consequence, of the value of unity frequency response at $\omega_o = 7$ rad/s, for the harmonic oscillator case (see Fig. 6). Thus, under the assumptions considered for Fig. 11-Scenario 1, the harmonic oscillator ensures asymptotic convergence, regardless of the specific value of $\lambda^\star$. Under the assumptions for Scenario 1, and as introduced in Eq. (10), the convergence error is shown in Fig. 12, where the grey lines denote the exponential convergence rate for each $\lambda^\star$. Therefore, perfect convergence is observed in all cases of the harmonic oscillator with perfect alignment between the definition of A_e and the spectral component ω_o, as evidenced by the error (e) approaching zero in Fig. 12.

Similarly, a special case, considering also Scenario 1 and an estimator based on the harmonic oscillator scheme with a mismatch between the harmonic component used in the definition of A_e and the peak frequency ω_o, is shown in Fig. 13, showing τ_e and $\tilde{\tau}_e$, obtained with $\lambda^\star = -10$ rad/s. In the instance shown in Fig. 13, A_e is defined using $\omega_p = 0.75\omega_o$, leading to a 25% mismatch between the definition of A_e and ω_o. Notably, Fig. 13 exhibits an absence of asymptotic behaviour, in contrast to the results illustrated in Fig. 11-top, for Scenario 1.

The results depicted in Scenario 2, illustrated in Fig. 11-middle, reveal that the harmonic oscillator fails to achieve perfect convergence, as observed in Scenario 1. However, the system demonstrates
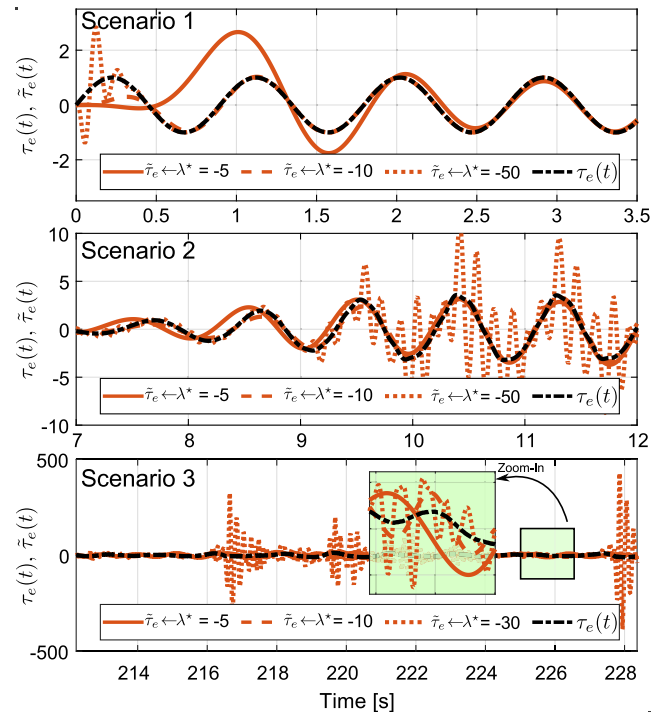

Fig. 11. Excitation torque estimates for the harmonic oscillator in Scenarios 1 (top), 2 (middle), and 3 (bottom). Closed-loop eigenvalues $\lambda^\star = -5, -10$, and -50 are considered for Scenarios 1 and 2, while $\lambda^\star = -5, -10$, and -30 are considered for Scenario 3.
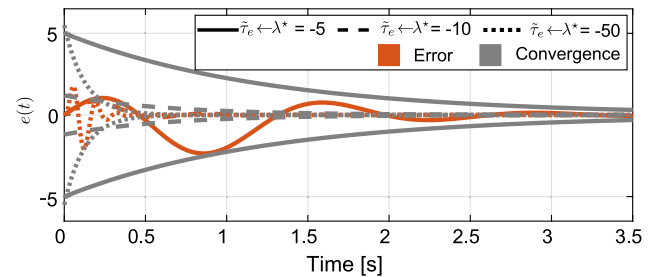

Fig. 12. Estimation error analysed for the harmonic oscillator case. The convergence rate is indicated for each case with grey lines.
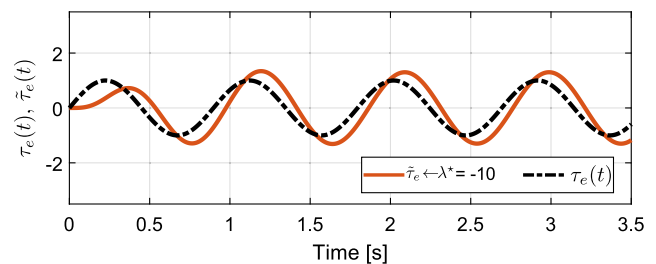

Fig. 13. Impact of a 25% mismatch between the definition of A_e and ω_o on estimation of the excitation torque.

adequate estimation performance, exhibiting a nearly negligible phase lag. Nevertheless, it is crucial to highlight the oscillatory response, which becomes particularly evident with $\lambda^\star = -50$ rad/s. The observed oscillatory response is a consequence of the amplification behaviour shown in Fig. 6, mainly between 10 and 200 rad/s. This amplification behaviour, coupled with the spectral content of the excitation signal, *i.e.* additional harmonics generated by harmonic contamination (see Fig. 7), leads to significant harmonic amplification and lack
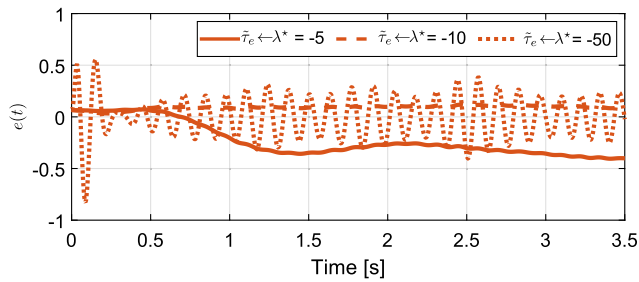
Fig. 14. Estimation error analysis for the harmonic oscillator case, when the prototype is experimentally excited with a monochromatic wave.

of asymptotic convergence. Therefore, there exists a trade-off, where the estimate error rate is limited by the pronounced amplification behaviour. This frequency domain behaviour has been theoretically analysed by Bode's sensitivity integral ('*waterbed effect*') (Goodwin et al., 2001).

From the results presented in Fig. 11-middle, the error signal is examined in Fig. 14, which implies a comparison between the excitation signal and its corresponding estimation. The error analysis, from Fig. 14, shows that limiting the analysis to the selected closed-loop eigenvalues, the best performance is obtained in Scenario 2 with $\lambda^\star = -10$. Additionally, the previously discussed amplification behaviour, is evident in the error assessment in Fig. 14, particularly with an amplified and oscillatory response obtained with $\lambda^\star = -50$. This behaviour significantly deviates $\tilde{\tau}_e$ from τ_e. However, it is crucial to note that, unlike the ideal case presented in Scenario 1 (see Fig. 11-top), in this scenario, the error does not converge asymptotically to zero. While this behaviour can be mitigated by including additional spectral components in A_e, adding the harmonic components visible in the frequency analysis of the excitation torque (see Fig. 7), this procedure introduces numerical complexity. Additionally, the complexity is further compounded by the fact that the exact spectral content is not readily accessible. Nonetheless, if the spectral components can be assumed as known, for each spectral component added to A_e, two extra modes are included in the augmented system (see Eq. (21)). Thus, the additional modes establish a trade-off for the harmonic oscillator, wherein performance is balanced against numerical complexity, particularly generated by matrix conditioning issues.

For Scenario 3. the time-domain results are shown in Fig. 11-bottom, where a close-up, indicated with a shadowed green box, is added to visualise the estimation results, regardless of the exaggerated dynamic range (close to 500 Nm). Despite restricting the closed-loop bandwidth with $\lambda^\star = -30$, it is evident, in Fig. 11-bottom, that the harmonic oscillator scheme, with fast closed-loop eigenvalues, produces substantial peaks (approaching 500 Nm) in $\tilde{\tau}_e$. The analysis of peaks introduced by exaggerated amplification can be effectively addressed, from a frequency domain perspective, similarly to Scenario 2. In Scenario 3, when the excitation signal undergoes the estimation process, the spectral content of the estimate is obtained by multiplying (in the frequency domain) the excitation signal (Fig. 8) with the estimation system frequency response (Fig. 9), which results in substantial spectral amplification, particularly in the band between 100 and 300 rad/s. It is clear that this amplification effect becomes more pronounced with fast closed-loop eigenvalues ($|\lambda^\star| > 30$ rad/s).

5.3.3. Error study

To quantitatively and comparatively evaluate the performance of the harmonic oscillator and the random walk schemes, particularly in the scenario involving a panchromatic wave, this study introduces a further analysis stage considering closed-loop eigenvalues in the following range:

$$|\lambda^\star| \in [0.1, 55] \quad \text{rad/s}. \tag{54}$$

In addition, three standard error measures are taken into account, namely: (i) Mean Squared Error (MSE); (ii) Normalised Root Mean Squared Error (NRMSE); and (iii) Normalised Mean Squared Error (NMSE) (The Mathworks Inc., 2024a). For precise definitions of these error measures, the interested reader is directed to the relevant source (The Mathworks Inc., 2024a). It is noteworthy that, though these are predominantly amplitude error metrics, they will also reflect phase errors, which it is known that wave energy controllers are sensitive to García-Violini et al. (2020). The outcomes of the error analysis are depicted in Fig. 15, featuring MSE, NRMSE, and NMSE in the left, middle, and right columns, respectively, each with a distinct title. From the results in Fig. 15, it can be noted that random walk estimation always betters the performance obtained with the harmonic oscillator. In the initial range of $\lambda^\star$ values, a notable and swift decrease in error is observed, particularly for the harmonic oscillator, extending from $|\lambda^\star| = 0.1$ to (approximately) $|\lambda^\star| = 3$ rad/s. This pronounced reduction is attributed to the dominance of initial transients, in the time domain responses, obtained with the initial values of $|\lambda^\star|$. However, for $\lambda^\star < -3$ rad/s, the error is primarily dictated by the steady-state response, rendering the impact of initial conditions negligible in comparison. Similarly, although with a lesser degree, the random walk exhibits a comparable phenomenon for $|\lambda^\star| = 0.1$ to (approximately) $|\lambda^\star| = 3$ rad/s, though with a slight inclination in the opposite direction.

With the three error measures, optimal performance is observed with the random walk scheme and closed-loop eigenvalues set at $\lambda^\star = -26.3$ rad/s. The disparities between the harmonic oscillator and random walk schemes are 49.9 dB, 24.96 dB, and 49.91 dB for the MSE, NRMSE, and NMSE error measures, respectively. It is important to note that employing a domain where $|\lambda^\star| > -60$ rad/s for the harmonic oscillator leads to numerical errors due to poor matrix conditioning. In a broader context, while the harmonic oscillator exhibits a slight advantage over the random walk (for $\lambda^\star \in [-19.3, -2.9]$ rad/s), the random walk scheme demonstrates superior performance beyond $\lambda^\star = -19.3$ rad/s compared to the harmonic oscillator. Specifically, concerning the normalised error measures (NRMSE and NMSE), the random walk manifests a negative value (in dB), indicating an error smaller than the reference excitation torque. In contrast, the harmonic oscillator consistently presents a positive normalised error value.

Finally, it should be noted that the discrepancy in Fig. 15 between the harmonic oscillator and the random walk for $|\lambda^\star| = 55$ rad/s stems from the greater amplification produced by the harmonic oscillator (see Fig. 9) compared to the random walk.

5.4. Discussion

Among the presented theoretical and practical findings, certain noteworthy observations merit emphasis. Firstly, it is demonstrated that the harmonic oscillator scheme aligns with the outcomes predicted by the IMP. However, this alignment is limited to WEC systems affected by ideal monochromatic waves, which lack practical relevance due to the exclusion of harmonic distortion and potential nonlinearities, existing in realistic (non-simulated) environments. Furthermore, the effective application of a harmonic oscillation estimation scheme mandates perfect knowledge of the spectral components of the wave excitation force/torque. However, such a circumstance is unrealistic and is typically confined to laboratory-scale experiments.

The amplified responses at high frequencies, as shown in Fig. 9, emphasise that the harmonic oscillator scheme can generate greater amplification than the random walk structure. Consequently, the random walk, imposing less amplification, exhibits superior performance when the spectral content of the excitation signal includes components that are substantially affected by the estimation system. On the contrary, the random walk scheme lacks a unitary frequency response at frequencies $\omega > 0$ rad/s. Due to the monochromatic spectral content of regular waves, the random walk fails to achieve optimal performance (convergence), characterised by an inherent phase lag. On the contrary,
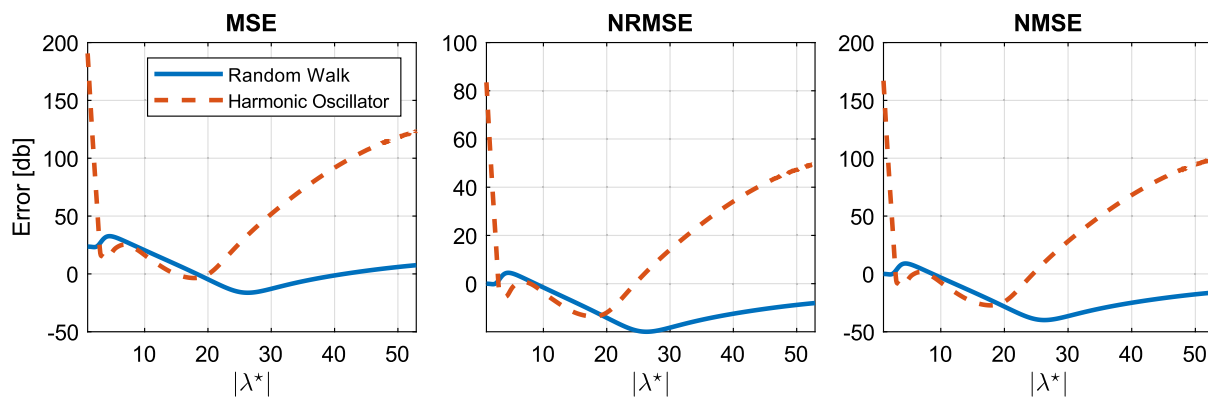
Fig. 15. MSE (left), NRMSE (middle), and NMSE (right) errors obtained with the harmonic oscillator (dashed) and the random walk (solid) for $|\lambda^\star| \in [0.1, 55]$ rad/s.

the harmonic oscillator structure achieves convergence with regular waves when appropriately designed (Fig. 11-top) but fails when poorly designed (Fig. 13), *i.e.* with a mismatch between the spectral content of the excitation signal and the disturbance model in A_e. This perspective sheds light on why the random walk model performs more effectively in irregular waves.

The analysis reveals that the harmonic oscillator, owing to the waterbed effect (Goodwin et al., 2001), generates regions of significant amplification. This amplification becomes critical in the presence of inherent measurement noise in experimental environments, harmonic distortion, and broadband processes, such as those observed in real, or panchromatic, waves. Furthermore, the harmonic oscillator substantially escalates numerical complexity, reaching a point where finding observer gains L becomes virtually impossible for high-magnitude closed-loop eigenvalues.

It is essential to note that, while various methods exist for computing observer gains (Bass–Gura, Ackermann, Riccati equation in a Kalman context with infinite estimation horizon, Lyapunov, etc.), numerical limitations persist across methodologies, regardless of their theoretical guarantees, which is extended to alternative design methodologies (optimal, such as LQG, or robust approaches, for example). In contrast, the estimator based on the random walk exhibits inferior performance in processes with monochromatic waves (ideal or experimental), but excels in scenarios involving real, panchromatic waves. Additionally, the design procedure for the random walk estimator is systematic, requiring no additional steps and incurring minimal computational cost (only adding one additional mode). In contrast, the harmonic oscillator requires the definition of a number (unknown) of spectral components and their specific location, with no theoretical guarantees of convergence or performance level, providing in some cases a substantial level of detrimental amplification.

It is important to emphasise that the considered assessment scenarios span the entire landscape theoretically addressed in this study. The study of steady-state behaviour is approached via perfectly periodic signals in both ideal and experimentally acquired excitation signal scenarios (Scenarios 1 and 2). The convergence conditions presented in the study are thus addressed through the exploration of these scenarios. The third scenario covers a fully realistic setting using a broadband JONSWAP-based excitation signal, where neither estimator achieves perfect convergence. However, the random walk, being the simplest structure, can be readily tuned for satisfactory performance.

To summarise, the family of estimators based on the IMP can be effectively described by the harmonic oscillator and random walk structures. Thus, the harmonic oscillator guarantees convergence under the assumptions of a band-limited perfectly periodic signal with its spectral components specifically defined in the disturbance model. This assures convergence, regardless of the chosen order or parameter values. However, the HO may introduce spectral amplification, affecting estimation performance, depending on the wave spectral characteristics. Conversely, the random walk structure can provide more favourable performance by reducing design demands and specifications.

6. Conclusion

This study highlights significant insights from both theoretical and practical perspectives in the estimation of wave excitation force/torque, considering the most established estimation methodologies. The rationale behind the harmonic oscillator estimation scheme is evident from an IMP theory perspective. However, this correspondence applies only to WEC systems influenced by polychromatic or monochromatic waves, a scenario lacking practical relevance due to the existence of potential harmonic distortion and nonlinearities in real-world and non-linear environments.

The study exposes that the harmonic oscillator induces spectral regions of notable amplification. This amplification becomes particularly problematic in the presence of inherent measurement noise in experimental settings, harmonic distortion, and broad-banded processes, as observed in real or panchromatic waves. Furthermore, the harmonic oscillator introduces significant numerical complexity, rendering the determination of observation gains L unattainable for high-magnitude closed-loop eigenvalues.

In direct comparison, the random walk estimation scheme surpasses the harmonic oscillator, mainly with panchromatic waves. The harmonic oscillator tends to amplify certain frequencies, leading to regions of significant signal amplification, particularly challenging in the presence of measurement noise, harmonic distortion, and broadband wave processes. In contrast, the random walk scheme proves more insensitive to these challenges. The systematic design methodology of the random walk, requiring minimal computational cost with the addition of just one extra mode, contributes to its effectiveness, making it a more robust choice in scenarios involving real, panchromatic, waves. This distinction underscores the practical advantages of the random walk estimation scheme over the harmonic oscillator.

Finally, it is crucial to highlight that the validity of the conclusions persists even in the presence of observation noise. Importantly, the analysis primarily focusses on an ideal sinusoidal excitation signal, free of noise. However, in the considered experimental scenarios, featuring periodic and JONSWAP-based waves, measurement noise is inherently involved. The outlined convergence conditions in this study hold when the excitation signal exhibits a finite number of discrete spectral components, explicitly included in model A_e. In addition, if a nonlinear effect induces periodic behaviour, such as harmonic distortion, and is appropriately accounted for in model A_e, the presented convergence conditions hold true.

CRediT authorship contribution statement

Demián García-Violini: Writing – review & editing, Writing – original draft, Software, Methodology, Formal analysis, Conceptualization. **Nicolás Faedo:** Writing – original draft, Methodology. **Yerai Peña-Sanchez:** Writing – review & editing, Validation, Methodology.

References

Abdelrahman, M., Patton, R., 2020. Observer-based unknown input estimator of wave excitation force for a wave energy converter. IEEE Trans. Control Syst. Technol. 28 (6), 2665–2672.

Ackermann, J., 1972. Der entwurf linearer regelungssysteme im zustandsraum. at-Automatisierungstechnik 20 (1–12), 297–300.

Chen, C.-T., 1999. Linear System Theory and Design. Oxford University Press.

Cummins, W.E., 1962. The impulse response function and ship motions. Schiffstechnik 47, 101–109.

Davis, A.F., Fabien, B.C., 2020. Wave excitation force estimation of wave energy floats using extended Kalman filters. Ocean Eng. 198, 106970.

Faedo, N., Peña-Sanchez, Y., Pasta, E., Papini, G., Mosquera, F.D., Ferri, F., 2023. SWELL: An open-access experimental dataset for arrays of wave energy conversion systems. Renew. Energy 212, 699–716.

Falnes, J., 2002. Ocean Waves and Oscillating Systems: Linear Interactions Including Wave-Energy Extraction. Cambridge Univ. Press.

Ferri, F., Sichani, M.T., Frigaard, P., 2012. A case study of short-term wave forecasting based on FIR filter: Optimization of the power production for the wavestar device. In: The Twenty-SEcond International Offshore and Polar Engineering Conference. OnePetro.

Folley, M., 2016. Numerical Modelling of Wave Energy Converters: State-of-The-Art Techniques for Single Devices and Arrays. Academic Press.

Francis, B.A., Wonham, W.M., 1976. The internal model principle of control theory. IEEE Trans. Autom. Control 21 (6), 457–465. http://dx.doi.org/10.1109/TAC.1976.1100705.

Garcia-Abril, M., Paparella, F., Ringwood, J.V., 2017. Excitation force estimation and forecasting for wave energy applications. IFAC-PapersOnLine 50 (1), 14692–14697.

García-Violini, D., Faedo, N., Jaramillo-Lopez, F., Ringwood, J.V., 2020. Simple controllers for wave energy devices compared. J. Mar. Sci. Eng. 8 (10), 793.

García-Violini, D., Peña-Sanchez, Y., Faedo, N., Bianchi, F., Ringwood, J.V., 2024. A model invalidation procedure for wave energy converters with experimental assessment and implications for control. Control Eng. Pract. 143, 105778.

García-Violini, D., Peña-Sanchez, Y., Faedo, N., Ferri, F., Ringwood, J.V., 2023. A broadband time-varying energy maximising control for wave energy systems (LiTe-Con+): Framework and experimental assessment. IEEE Trans. Sustain. Energy 1–10. http://dx.doi.org/10.1109/TSTE.2023.3237023.

García-Violini, D., Peña-Sanchez, Y., Faedo, N., Windt, C., Ferri, F., Ringwood, J.V., 2021. Experimental implementation and validation of a broadband LTI energy-maximizing control strategy for the wavestar device. IEEE Trans. Control Syst. Technol. 29 (6), 2609–2621.

Goodwin, G.C., Graebe, S.F., Salgado, M.E., et al., 2001. Control System Design, vol. 240, Prentice Hall New Jersey.

Guo, B., Ringwood, J.V., 2021. A review of wave energy technology from a research and commercial perspective. IET Renew. Power Gener. 15 (14), 3065–3090.

Hansen, R.H., Kramer, M.M., 2011. Modelling and control of the wavestar prototype. In: Proc. EWTEC. Southampton, UK.

Hasselmann, K., 1973. Measurements of wind wave growth and swell decay during the Joint North Sea Wave Project (JONSWAP). Deutches Hydrographisches Institut 8, 95.

Hillis, A., Brask, A., Whitlam, C., 2020. Real-time wave excitation force estimation for an experimental multi-DOF WEC. Ocean Eng. 213, 107788.

International Energy Agency, 2019. World energy outlook 2019. URL https://www.iea.org/reports/world-energy-outlook-2019.

Kracht, P., Perez-Becker, S., Richard, J.-B., Fischer, B., 2015. Performance improvement of a point absorber wave energy converter by application of an observer-based control: Results from wave tank testing. IEEE Trans. Ind. Appl. 51 (4), 3426–3434.

Krener, A.J., 2003. The Convergence of the Extended Kalman Filter. Springer.

LHEEA, N.-P., 2017. Laboratoire de Recherche en Hydrodynamique Énergetique et Environnement Atmospherique. https://goo.gl/yX8nFu. (Online Accessed 14 March 2024).

Li, D., Patton, R., 2023. Model predictive energy-maximising tracking control for a wavestar-prototype wave energy converter. J. Mar. Sci. Eng. 11 (7), 1289.

Ling, B.A., Batten, B.A., 2015. Real time estimation and prediction of wave excitation forces on a heaving body. In: International Conference on Offshore Mechanics and Arctic Engineering, vol. 56574, American Society of Mechanical Engineers, V009T09A017.

Luenberger, D.G., 1964. Observing the state of a linear system. IEEE Trans. Milit. Electron. 8 (2), 74–80.

Luenberger, D., 1971. An introduction to observers. IEEE Trans. Autom. Control 16 (6), 596–602.

Nguyen, H.-N., Sabiron, G., Tona, P., Kramer, M.M., Vidal Sanchez, E., 2016. Experimental validation of a nonlinear MPC strategy for a wave energy converter prototype. In: International Conference on Offshore Mechanics and Arctic Engineering, vol. 49972, American Society of Mechanical Engineers, V006T09A019.

Nguyen, H.-N., Tona, P., 2018. Wave excitation force estimation for wave energy converters of the point-absorber type. IEEE Trans. Control Syst. Technol. 26 (6), 2173–2181.

Peña-Sanchez, Y., Faedo, N., Ringwood, J.V., 2019a. A critical comparison between parametric approximation methods for radiation forces in wave energy systems. In: ISOPE International Ocean and Polar Engineering Conference. ISOPE, pp. ISOPE–I.

Peña-Sanchez, Y., Windt, C., Davidson, J., Ringwood, J.V., 2019b. A critical comparison of excitation force estimators for wave-energy devices. IEEE Trans. Control Syst. Technol. 28 (6), 2263–2275.

Rhudy, M.B., Gu, Y., 2013. Online stochastic convergence analysis of the Kalman filter. Int. J. Stoch. Anal. 1–9.

Ringwood, J.V., Bacelli, G., Fusco, F., 2014. Energy-maximizing control of wave-energy converters: The development of control system technology to optimize their operation. IEEE Control Syst. 34 (5), 30–55.

The Mathworks Inc., 2024a. GoodnessOfFit: Documentation. . (Online Accessed 14 March 2024).

The Mathworks Inc., 2024b. MATLAB. https://www.mathworks.com. (Accessed: 12 March 2024).

Zhang, Z., Qin, J., Wang, D., Wang, W., Liu, Y., Xue, G., 2023. Research on wave excitation estimators for arrays of wave energy converters. Energy 264, 126133.